

Results from an Einstein@Home search for continuous gravitational waves from Cassiopeia A and Vela Jr. using LIGO O2 data

JORGE MORALES,^{1,2,3} JING MING,^{3,4} MARIA ALESSANDRA PAPA,^{3,4} HEINZ-BERND EGGENSTEIN,^{3,4} AND
BERND MACHENSCHALK^{3,4}

¹ Center for the Exploration of Energy and Matter and Department of Physics, Indiana University, Bloomington, IN 47405, USA

² Physics Department, Indiana University, Bloomington, IN, 47405, USA

³ Max Planck Institute for Gravitational Physics (Albert Einstein Institute), Callinstrasse 38, 30167, Hannover, Germany

⁴ Leibniz Universität Hannover, D-30167 Hannover, Germany

ABSTRACT

We conduct two searches for continuous, nearly monochromatic gravitational waves originating from the central compact objects in the supernova remnants Cassiopeia A and Vela Jr. using public LIGO data. The search for Cassiopeia A targets signal frequencies between 20 Hz and 400 Hz; the Vela Jr. search between 400 Hz and 1700 Hz, and both investigate the broadest set of waveforms ever considered with highly sensitive deterministic search methods. Above 1500 Hz the Vela Jr. search is the most sensitive carried out thus far, improving on previous results by over 300%. Above 976 Hz these results improve on existing ones by 50%. In all we investigate over 10^{18} waveforms, leveraging the computational power donated by thousands of Einstein@Home volunteers. We perform a 4-stage follow-up on more than 6 million waveforms. None of the considered waveforms survives the follow-up scrutiny, indicating no significant detection candidate. Our null results constrain the maximum amplitude of continuous signals as a function of signal frequency from the targets. The most stringent 90% confidence upper limit for Cas A is $h_0^{90\%} \approx 7.3 \times 10^{-26}$ near 200 Hz, and for Vela Jr. it is $h_0^{90\%} \approx 8.9 \times 10^{-26}$ near 400 Hz. Translated into upper limits on the ellipticity and r-mode amplitude, our results probe physically interesting regions: for example the ellipticity of Vela Jr. is constrained to be smaller than 10^{-7} across the frequency band, with a tighter constraint of less than 2×10^{-8} at the highest frequencies.

Keywords: gravitational waves; supernova remnants; neutron stars

1. INTRODUCTION

Continuous gravitational waves are weak and persistent quasi-monochromatic signals that remain undetected. Continuous waves are believed to be orders of magnitude weaker than transient gravitational waves resulting from mergers of binary systems of black holes and/or neutron stars. This inherent weakness poses a significant challenge in their detection. On the other hand, continuous waves are thought to persist for years so the data can be integrated over many months against the expected signal templates to amplify the signal-to-noise ratio and enhance our ability to detect the signal.

Broadly speaking, there are three types of continuous wave searches. Targeted searches focus on continuous

waves from pulsars with known electromagnetic spin frequency and its evolution (B. P. Abbott et al. 2019a,b; R. Abbott et al. 2022a,b; L. Nieder et al. 2020; B. Rajbhandari et al. 2021; C. J. Clark et al. 2023; B. J. Owen et al. 2024; A. Ashok et al. 2021, 2024; L. Mirasola et al. 2024; A. G. Abac & other 2025). These are the most sensitive and least computationally expensive continuous wave searches. In contrast, all-sky searches aim for continuous waves from unknown sources across a significant portion of the sky (V. Dergachev & M. Papa 2020; V. Dergachev & M. A. Papa 2021; A. Singh & M. A. Papa 2023; P. B. Covas et al. 2022, 2024; R. Abbott et al. 2022c; B. Steltner et al. 2023; V. Dergachev & M. A. Papa 2023). The broad parameter space that all-sky searches need to cover makes them the least sensitive and most computationally expensive. Somewhere in between, directed searches look for continuous waves from sources at compelling sky locations where no elec-

tromagnetic pulsations have been detected (B. P. Abbott et al. 2019c,d; V. Dergachev et al. 2019; J. Ming et al. 2019; M. A. Papa et al. 2020; O. J. Piccinni et al. 2020; M. Millhouse et al. 2020; L. Lindblom & B. J. Owen 2020; Y. Zhang et al. 2021; R. Abbott et al. 2021a, 2022d,e,f; B. J. Owen et al. 2022; J. Ming et al. 2022; J. Wang & K. Riles 2024; J. Ming et al. 2024). Given the absence of prior knowledge about the frequency and its evolution, directed searches require convolving the data with a vast array of signal waveforms, incurring a high computational cost.

Continuous waves can arise from dynamics deviating from axial symmetry within the interior of rotating neutron stars (where the axis of symmetry is the rotation axis). These dynamics include sustained deformations in the neutron star crust, informally known as “mountains” (G. Ushomirsky et al. 2000; B. Haskell et al. 2006; F. Gittins et al. 2021; F. Gittins & N. Andersson 2021; T. J. Hutchins & D. I. Jones 2023; J. A. Morales & C. J. Horowitz 2022, 2024), and periodic non-radial oscillations of dense fluids within neutron stars, referred to as r-modes or Rossby waves (N. Andersson et al. 1999; E. F. Brown & G. Ushomirsky 2000; B. Haskell et al. 2014; F. Gittins & N. Andersson 2023). Additionally, continuous waves may be generated through more exotic mechanisms, like the rapid inspiral of two compact dark-matter objects (C. J. Horowitz & S. Reddy 2019; C. Horowitz et al. 2020; A. L. Miller et al. 2024) and the super-radiant emission of axion-like particles around spinning black holes (A. Arvanitaki et al. 2015; S. J. Zhu et al. 2020; R. Abbott et al. 2022g; L. Mirasola et al. 2025).

In the current study, we perform directed searches on Cassiopeia A (G111.7-2.1) and Vela Jr. (G266.2-1.2). These are two galactic compact objects that reside at the center of young and nearby supernova remnants. These central compact objects are presumed rapidly spinning, isolated neutron stars that harbor most of the angular momentum of their respective progenitors. If these central objects are indeed rapidly rotating neutron stars with significant mountains or r-mode oscillations, a fraction of the substantial angular momentum reservoir is being radiated as continuous waves.

We implement our searches within the Einstein@Home volunteer distributed computing project (Einstein@Home 2023), with a computing budget spanning several months. The selection of our two targets and their search setups results from an optimization scheme that identifies the sources and search setups that maximize the detection probability within a specified computational budget (J. Ming et al. 2016, 2018). This scheme incorporates factors such as the

sensitivity and computing cost of the search pipeline, the age and distance of a source, and priors on the source’s frequency, frequency derivatives, and ellipticity. The search sensitivity depends on the search setup and on the noise level in detectors’ data. We conduct the post-processing of the results of the Einstein@Home searches using the in-house Atlas super-computing cluster (AEI 2023) to further enhance sensitivity.

2. TARGETS

2.1. *Cassiopeia A* (G111.7-2.1)

Cassiopeia A (Cas A) is the central compact object resulting from one of the most recent galactic core-collapse supernovae. It is at the center of the supernova remnant CXOU J232327.9+584842, and its position was measured using Chandra X-ray satellite data (H. Tananbaum 1999). The prevailing consensus is that this explosive event occurred 310-350 years ago (R. A. Fesen et al. 2006) at a distance of 3.3-3.7 kpc from Earth (J. E. Reed et al. 1995). The age and distance are calculated using the observed expansion rate of the outer ejecta of the remnant and the radial velocity of its central compact object. Based on its X-ray spectrum, W. Ho & C. Heinke (2009) suggest that the central object is neutron star with a carbon atmosphere and a small magnetic field. The intricate and asymmetric nebula surrounding Cas A is a potential fingerprint of an asymmetric neutron star interior. Additionally, if the newly born neutron star was fast-spinning and with a relatively weak internal magnetic field as W. Ho & C. Heinke (2009) suggest, it might well be subject to rotational instabilities like r-modes (B. J. Owen et al. 1998).

2.2. *Vela Jr.* (G266.2-1.2)

The X-ray-to-optical-flux ratio reveals that Vela Jr. is the central compact object of the supernova remnant CXOU J085201.4-461753. Its position was originally pin-pointed by the Chandra X-ray satellite (G. G. Pavlov et al. 2001), with subsequent infra-red observations confirming the position and suggesting that the central compact object is a neutron star (Mignani, R. P. et al. 2007).

Based on Ti^{44} line emission from the supernova remnant the age of the remnant is estimated to be 700 yrs and its distance to be 200 pc (A. F. Iyudin et al. 1998). Conversely Chandra X-ray data and hydrodynamic analyses of the expansion of the remnant indicate an older and more distant object, with an age of 4300 yrs and a distance of 750 pc (G. E. Allen et al. 2014).

3. THE SIGNAL MODEL

For any plane gravitational wave, there exists a frame that satisfies three key conditions: (1) it is station-

ary relative to its source, (2) it is perpendicular to the direction of propagation, and (3) it lies parallel to the polarization plane of the wave. In this frame, the gravitational-wave strain can be expressed as a linear combination of two polarizations, denoted as h_+ and h_\times :

$$h_+(t) = A_+ \cos \Phi(t), \quad (1)$$

$$h_\times(t) = A_\times \sin \Phi(t). \quad (2)$$

$\Phi(t)$ is the gravitational-wave phase and $A_{+,\times}$ denote the gravitational-wave polarization amplitudes:

$$A_+ = \frac{1}{2} h_0 (1 + \cos^2 \iota), \quad (3)$$

$$A_\times = h_0 \cos \iota, \quad (4)$$

where ι represents the angle between the angular momentum of the neutron star and the line of sight from Earth, while h_0 is the intrinsic continuous wave amplitude.

The frequency of a continuous wave emitted by an isolated rapidly rotating neutron star evolves gradually over time, and its temporal behaviour can be described using a Taylor expansion around a reference time in the Solar System Barycenter (SSB) τ_0 :

$$f(\tau) = f_0 + \dot{f}_0(\tau - \tau_0) + \frac{1}{2} \ddot{f}_0(\tau - \tau_0)^2. \quad (5)$$

The continuous wave strain at the detector takes the form

$$h(t) = F_+(\alpha, \delta, \psi; t) h_+(t) + F_\times(\alpha, \beta, \psi; t) h_\times(t), \quad (6)$$

where $F_{+,\times}(\alpha, \delta, \psi; t)$ are the beam-pattern functions, α and δ represent the right ascension and declination of the source, ψ is for the orientation angle of the wave-frame with respect to the detector frame, and t denotes the time in the detector frame. The conversion from the detector frame time t to the SSB frame time τ is determined by

$$\tau(t) = t + \frac{\vec{r}(t) \cdot \hat{n}}{c} + \Delta_{E\odot} - \Delta_{S\odot}, \quad (7)$$

where \vec{r} is the detector position vector, \hat{n} is the unit vector pointing towards the source from the SSB, and $\Delta_{E\odot}$ and $\Delta_{S\odot}$ are the Einstein and Shapiro time delays, respectively.

4. THE DATA

In the Einstein@Home searches, we analyze public data obtained during the second observing run (O2) of the two LIGO detectors, taken between GPS times 1167993370 (January 9, 2017) and 1187731774 (August

25, 2017) (R. Abbott et al. 2021b). During this period, the Hanford, Washington detector exhibited a duty cycle of 65 %, while the Livingston, Louisiana detector had a duty cycle of 62%. In the post-processing of the Einstein@Home search results, we use public data obtained during the first half of the third observing run (O3a) of the two LIGO detectors, taken between GPS times 1238421231 (April 04 2019) and 1253973231 (October 01 2019) (R. Abbott et al. 2023). Duty factors of detectors of Hanford and Livingston during this period are 71% for and 76% respectively. The O2 and O3a search reference times we adopt are $\tau_{\text{SSB}}^{\text{O2}} = 1177858472.0$ and $\tau_{\text{SSB}}^{\text{O3a}} = 1246197626.5$. We generate Short Fourier Transforms of data segments, each spanning 1800 seconds. We eliminate data affected by artifacts such as calibration lines and main power lines, as well as loud transient glitches (B. Steltner et al. 2022b).

5. THE EINSTEIN@HOME SEARCH

We employ a “stack-slide” approach for semi-coherent searches (P. R. Brady et al. 1998; P. R. Brady & T. Creighton 2000), leveraging the Global Correlation Transform (GCT) method (H. J. Pletsch 2008; H. J. Pletsch & B. Allen 2009; H. J. Pletsch 2010). In this type of search, the dataset, which spans a total observing time T_{obs} , is partitioned into shorter N_{seg} segments of equal span T_{coh} . The data in each segment i is analyzed coherently. Afterwards, the coherent detection statistics \mathcal{F}_i from all the segments are summed. The coherent detection statistic from each segment is a matched filter between the data and a waveform model with parameters $\{f, \dot{f}, \ddot{f}, \alpha, \delta\}$. The final detection statistic is

$$\bar{\mathcal{F}} = \frac{1}{N_{\text{seg}}} \sum_{i=1}^{N_{\text{seg}}} \mathcal{F}_i. \quad (8)$$

In the ideal scenario of Gaussian noise, $N_{\text{seg}} \bar{\mathcal{F}}$ follows a chi-squared distribution with $4N_{\text{seg}}$ degrees of freedom and a non-centrality parameter $\rho^2 = \sum_i \rho_i^2$, the sum of the squared signal-to-noise ratios from the individual segments. In each segment $\rho_i^2 \propto \frac{h_0^2 T_{\text{coh}}}{S_h}$, where S_h is the strain power spectral density of the noise at the signal’s frequency (P. Jaranowski et al. 1998).

While many disturbances are mitigated with the data preparation techniques (B. Steltner et al. 2022b), some spectral lines persist. These residual lines can elevate the values of $\bar{\mathcal{F}}$ for search templates that use data affected by those disturbances. For this reason, a line robust detection statistic $\hat{\beta}_{\text{S/GLtL}}$ is used to rank the Einstein@Home search results. This detection statistic is the log of a Bayesian odds ratio that tests the signal (S) hypothesis versus an extended noise hypothesis. The

extended noise hypothesis considers Gaussian (G) noise or line-noise (L) or transient-line noise (tL) (D. Keitel et al. 2014; D. Keitel 2016). The usage of $\hat{\beta}_{\text{S/GLtL}}$ as a ranking detection statistic reduces the incidences of false alarms caused by noise that resembles a continuous wave more than it resembles Gaussian noise.

The search setup consists of the coherent baseline time T_{coh} , the signal-parameter ranges and the grid-spacings of the templates δf , $\delta \dot{f}$ and $\delta \ddot{f}$. For each of the searches, the grid-spacings in frequency and spindown parameters over the parameter space are constant. Every search setup has an associated average mismatch \bar{m} , which measures the average loss in signal-to-noise ratio due to the mismatch between the parameters of a signal and the closest (f , \dot{f} and \ddot{f}) grid point. The search setups are given at the top of Table 1.

The search ranges of the spin-down parameters are frequency-dependent, as first proposed by K. Wette et al. (2008). We use different search ranges for Cas A and Vela Jr.:

$$\begin{cases} 20 \text{ Hz} & \leq f \leq 400 \text{ Hz} & \text{for Cas A} \\ 400 \text{ Hz} & \leq f \leq 1700 \text{ Hz} & \text{for Vela Jr.} \\ -f/\tau & \leq \dot{f} \leq 0 \text{ Hz/s} \\ 0 \text{ Hz/s}^2 & \leq \ddot{f} \leq 7 f/\tau^2 \end{cases} \quad (9)$$

where $\tau = 330$ years and $\tau = 700$ years are the ages of Cas A and Vela Jr., respectively. The choice of the 700 years age for Vela Jr. produces the broadest \dot{f} and \ddot{f} search ranges, and it is hence the safest choice. The ranges for \dot{f} and \ddot{f} defined above encompass waveforms from all emissions mechanisms with braking index $n \leq 7$, and more. In fact Eq.s 9 further expand the template bank in two ways: 1) extending the ranges of \dot{f} and \ddot{f} to 0, 2) not requiring consistency between the underlying braking index of the \dot{f} and \ddot{f} values. We make this choice because it is easy to implement within the search pipeline and because indications exist that a strict power law frequency evolution, especially in young pulsars, may not be completely adequate to describe the observations – see for instance A. F. Vargas & A. Melatos (2024) and references therein.

The two searches are deployed on the Einstein@Home volunteer computing project, which is built on the BOINC (Berkeley Open Infrastructure for Network Computing) architecture (D. Anderson 2004; D. P. Anderson et al. 2006). Einstein@Home uses the idle time of volunteer computer to search for weak astrophysical signals from neutron stars, including continuous waves. In total among the two targets, $\approx 1.3 \times 10^{18}$ waveform templates are searched. 92% of the templates are used in the search for Vela Jr., because of the broad frequency range.

The total workload is divided into work-units whose size is chosen to keep the volunteer computer busy for ≈ 8 CPU hours, resulting in a grand total of 5.7 million work units.

The number of templates searched at a given frequency increases with frequency due to the frequency-dependent search ranges of \dot{f} and \ddot{f} (Eq.s 9). Figure 1 shows the number of templates searched in 1-Hz bands as a function of frequency for the two targets.

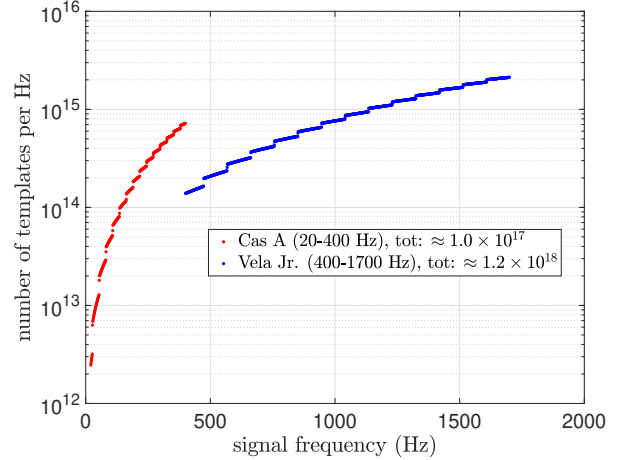


Figure 1. Number of templates searched in 1-Hz bands as a function of signal frequency. In the legend we also show the total number of templates searched for each search.

6. POST-PROCESSING OF EINSTEIN@HOME RESULTS

6.1. Overview

Each Einstein@Home work-unit returns the 10 000 most significant results. The 5.7 million work units hence return in all 57 billion candidates.

The significance of results calculated on the volunteer computers is expressed by the value of the $\hat{\beta}_{\text{S/GLtL}}$ detection statistic. The larger this value is, the most likely it is that the candidate is associated with an astrophysical signal. The values of $\hat{\beta}_{\text{S/GLtL}}$ at a certain parameter grid point are actually approximations. This approximation reduces the computational cost of Einstein@Home searches significantly, but incurs a loss. For the most significant work-unit results the non-approximated value is computed. We indicate the re-computed detection statistics with a subscript “r” as in “re-computed”: $\hat{\beta}_{\text{S/GLtLr}}$ and $\bar{\mathcal{F}}_r$. The value of the recomputed statistics is expected to increase in comparison to the non-recomputed value if the waveform template of a candidate is associated to a continuous-wave signal within the data.

Stage	T_{coh}	N_{seg}	δf	$\delta \dot{f}$	$\delta \ddot{f}$	\bar{m}
E@H (Cas A)	240 hr	17	4.9×10^{-7} Hz	8.3×10^{-14} Hz/s	3.4×10^{-20} Hz/s ²	14.3%
E@H (Vela Jr.)	240 hr	17	4.0×10^{-7} Hz	8.3×10^{-14} Hz/s	2.7×10^{-20} Hz/s ²	10.5%
1	1080 hr	5	1.3×10^{-7} Hz	1.5×10^{-14} Hz/s	1.2×10^{-20} Hz/s ²	13.3 %
2	2760 hr	2	3.5×10^{-8} Hz	2.2×10^{-15} Hz/s	1.2×10^{-21} Hz/s ²	7.6 %
3	5496 hr	1	9.6×10^{-9} Hz	2.9×10^{-15} Hz/s	1.5×10^{-21} Hz/s ²	2.0 %
4 (new data)	1440 hr	3	6.7×10^{-8} Hz	1.2×10^{-14} Hz/s	1.6×10^{-21} Hz/s ²	5.4 %

Table 1. Search setups used. The Einstein@Home searches (“E@H”) are different for the two targets whereas the follow-up Stages 1-4 use the same setup for both targets. T_{coh} is the coherent baseline time, N_{seg} is the number of coherent segments, δf , $\delta \dot{f}$, and $\delta \ddot{f}$ are the grid-spacings of the templates, and \bar{m} is the average mismatch.

Cas A						
Stage	Δf [Hz]	$\Delta \dot{f}$ [Hz/s]	$\Delta \ddot{f}$ [Hz/s ²]	R_{thr}^a	N_{in}	N_{out}
E@H	full range	full range	full range	-	1.0×10^{17}	1,516,000
1	1.2×10^{-6}	1.4×10^{-13}	4.2×10^{-20}	1.8	1,516,000	801,589
2	3.0×10^{-7}	3.3×10^{-14}	1.1×10^{-20}	4.9	801,589	102,661
3	6.5×10^{-8}	4.4×10^{-15}	3.3×10^{-21}	9.0	102,661	45,483
4 (new data)	$> 3.2 \times 10^{-8}$	$> 4.8 \times 10^{-15}$	3.1×10^{-21}	3.5	45,483	0
Vela Jr.						
Stage	Δf [Hz]	$\Delta \dot{f}$ [Hz/s]	$\Delta \ddot{f}$ [Hz/s ²]	R_{thr}^a	N_{in}	N_{out}
E@H	full range	full range	full range	-	1.2×10^{18}	5,199,849
1	6.3×10^{-6}	6.1×10^{-14}	2.3×10^{-20}	1.9	5,199,849	1,822,369
2	2.9×10^{-7}	9.3×10^{-14}	1.3×10^{-20}	5.0	1,822,369	202,655
3	5.3×10^{-8}	5.9×10^{-14}	3.4×10^{-21}	9.4	202,655	70,259
4 (new data)	$> 3.0 \times 10^{-8}$	$> 4.7 \times 10^{-15}$	2.9×10^{-21}	3.1	70,259	0

Table 2. Δf , $\Delta \dot{f}$, and $\Delta \ddot{f}$ indicate the extent of the search regions per candidate for Stages 1-4 and for the original Einstein@Home (E@H) search. For Stage 4 the extents represent the non-evolved uncertainties, since the evolved ones vary depending on the parameters of the specific candidate. N_{in} represents the number of candidates searched for Stages 1-4 and the total number of templates for the E@H search. N_{out} is the number of surviving candidates from each stage. R_{thr}^a is the threshold of Eq. 11 for Stages a=1-4. The results from the E@H search are selected based on the pixeling procedure described in Section 6.3 and hence the R_{thr} value is irrelevant.

Once the detection statistics are re-computed for the 5.7×10^{10} most significant Einstein@Home results, we proceed to select the ones that we will follow-up using the *pixeling procedure* described in section 6.3. These constitute the “Stage-0 candidates”.

The central idea of the follow-up searches is to increase the length of the coherent segments to accumulate more signal-to-noise ratio for candidates associated with astrophysical signals. We define

$$R^a \equiv \frac{2\bar{\mathcal{F}}_r^{\text{Stage-a}} - 4}{2\bar{\mathcal{F}}_r^{\text{Stage-0}} - 4} \quad \text{for } a = 1 \dots 4 \quad (10)$$

which quantifies how much the excess in squared signal-to-noise ratio estimated from the Stage-a candidate ($2\bar{\mathcal{F}}_r^{\text{Stage-a}} - 4$), compares to the excess estimated for the same candidate at Stage-0. Since the square of signal-to-noise ratio of a signal is roughly proportional to the coherent baseline time T_{coh} of the data segments, if T_{coh}

increases, it is expected that R^a will also increase. We set a threshold value R_{thr}^a and

$$\text{if } R^a < R_{\text{thr}}^a \rightarrow \text{candidate discarded.} \quad (11)$$

Similar to J. Ming et al. (2024), R_{thr}^a is determined by requiring that it is safe against discarding signals from our target population (see next Section). So thousands of test signals from the target population are added to the data, each is searched for, exactly as done for the real search, and the corresponding R^a is measured. The threshold dismisses at each stage less than 0.01% of the test signals, resulting in an overall false dismissal of less than 0.04%.

The candidates from this recovery study of signals from the target population also serve a crucial role in determining the region around candidates that must be searched at each stage. This region has been known in

the literature as “containment region”. The containment region is defined by a triplet of values at each stage, Δf^a , $\Delta \dot{f}^a$, and $\Delta \ddot{f}^a$, such that candidates from the target population at that stage are recovered within this distance from the real parameter values. The containment region around the candidates’ parameters at Stage-a is the search region at Stage-a+1. Tables 2 list the search regions at each stage.

6.2. Target population

The post-processing procedures that follow the Einstein@Home search have been designed to have a very low false dismissal for signals of the target population. The target population signals for a given supernova remnant obviously all come from the position of that source and have frequency and frequency derivative values in the target range, randomly displaced from the search grid points. The $\cos \iota$ and ψ parameters are uniformly distributed $-1 \leq \cos \iota \leq 1$, $-\pi/4 \leq \psi \leq \pi/4$. The signal strength is set to the target strength with respect to the amplitude spectral density: the target population signals have amplitudes corresponding to $\mathcal{D} = 90 [1/\sqrt{\text{Hz}}]$ for both Vela Jr. and Cas A (see Eq. 15 for the relation between the amplitude h_0 and \mathcal{D}). The target depth value is the best (i.e. highest sensitivity) that we could achieve with the available computational power, and in absolute terms it is the highest achieved on such a large parameter space.

6.3. Stage-0

The goal at this stage is to efficiently select the most compelling candidates from the 5.7×10^{10} results returned to the Einstein@Home server. Historically, there have been three main ways to achieve this.

The first method involves setting a desired threshold on the detection statistic and selecting the search candidates whose detection statistic lies above that threshold. This approach is straightforward and time-saving. However the number of selected candidates from disturbed frequency bands may greatly exceed those in undisturbed bands leading to a computationally wasteful and less effective follow-up process.

The second method is to select a fixed number of candidates per frequency band. The fixed number of selected candidates per band is determined by the available computational budget. We call this method to select follow-up candidates method “simple thresholding”. In each band, this method selects a fixed amount of candidates, with the quietest candidate setting the detection statistic threshold. Unfortunately, in disturbed bands, this procedure might only select candidates associated with disturbances and discard interesting candidates not linked to the disturbance.

The third method is called *clustering*. In clustering, candidates associated with the same astrophysical or non-astrophysical causes are identified, and one of them is chosen (A. Singh et al. 2017; B. Steltner et al. 2022a). Clustering is generally efficient because it prevents the waste of resources on following up candidates origination from the same root cause. While clustering has proven to be very effective in all-sky searches, in directed searches, the sensitivity improvement compared with simple thresholding is very modest – less than 1 % (J. Ming et al. 2024). Since determining a good operating point for the clustering procedure requires time and extensive Monte Carlos, we do not pursue it here. Instead, we propose an alternative scheme to select the Stage-0 results to follow-up: the pixeling procedure. This alternative is straightforward and efficient and does not loose detection efficiency in disturbed frequency bands.

6.3.1. The Pixeling Procedure

We divide the searched frequency range in N_{bands} bands of equal size. For each frequency band, we consider N_p frequency-spindown “pixels”, with each pixel being a unique small region of the searched parameter space. The frequency range covered by each pixel is 5 mHz. The \dot{f} range covered by a pixel varies with frequency and with the age τ of the source, and it is equal to $f/10\tau$. So we consider 0.5 Hz wide frequency bands, and $N_p = 100 \times 10$ pixels to cover the $f \times \dot{f}$ parameter space.

We take the top $n_{px} = 2$ Stage-0 results from waveforms with parameters in each pixel, with n_{px} determined by the available computational budget for the follow-up. We call these *candidates*. The lowest detection statistic in the pixels from a 50 mHz region is shown in Figure 2 as an example.

In all we select ≈ 1.5 million candidates from the Cas A search and ≈ 5.2 million from Vela Jr. search. Both these numbers are $< 2N_p \times N_{\text{bands}}$ (twice the total number of pixels) because not all pixels contribute 2 candidates – in fact some contribute no candidate at all. This is due to the fact that the original results are themselves top-lists returned by the Einstein@Home volunteer computers, and in the presence of very large disturbances most results might be concentrated in certain frequency-spindown regions rather than being \approx uniformly distributed among the pixels. The average value of the $\hat{\beta}_{\text{S/GLtLr}}$ detection statistic of the considered candidates increases by 4 going from 20 to 400 Hz for Cas A and increases by 2 going from 400 to 1700 Hz for Vela Jr. This is due to the a trials factor effect: we are taking the most

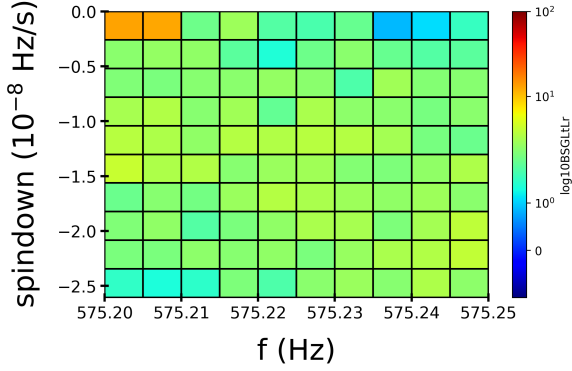


Figure 2. An example of the lowest recorded $\hat{\beta}_{S/GLTLR}$ per pixel in a slightly disturbed (top-left) band. The results shown come from the Vela Jr. search. Each cell in this figure is a “pixel”.

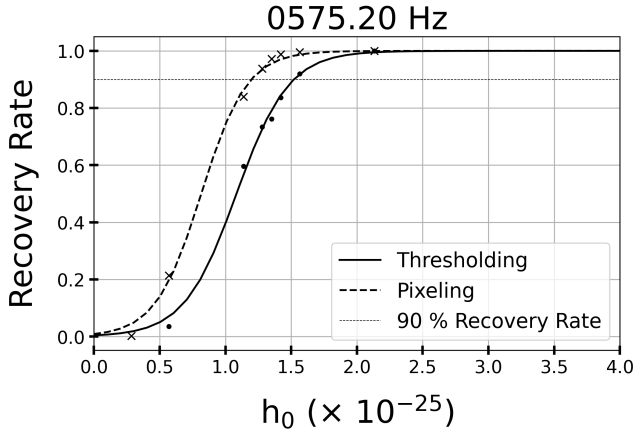


Figure 3. Comparison between the performance of the pixeling and the simple thresholding selection methods of the example slightly disturbed band.

significant 2 results from a parameter space (the pixel) that increases in size as the frequency increases.

Compared to simple thresholding at fixed number of selected candidates, in well-behaved, nearly Gaussian noise, the pixeling procedure and simple thresholding yield comparable results. When the data is affected by disturbances pixeling is never worse than simple thresholding and for most disturbances, which are localized in $f - \hat{f}$, the detection efficiency is enhanced with pixeling. In Figure 3, that features data with a typical disturbance, the 90% detection efficiency amplitude is $\approx 1.2 \times 10^{-25}$ using the pixeling method, and $\approx 1.6 \times 10^{-25}$ using the simple thresholding method.

6.4. Stages 1-4

We follow-up the candidates selected through the pixeling procedure with a cascade of three semi-coherent searches with increasing coherent time and decreasing

mismatch. The surviving candidates are verified on a different data set, that data from the first half of the O3 run, O3a. The searched volume around the nominal candidate parameters at each stage is detailed in Tables 2. The search region for the O3a search is the containment region from the O2 search evolved to the time of the O3a data (see the details of Eq. 10 in J. Ming et al. (2024)).

The search setups are determined by their effectiveness and safety in separating noise from signals and by computational feasibility. The effectiveness and safety of the thresholds on the R_{thr}^a are established based on the distributions shown in Figures 4.

The number of candidates fed to each stage and the surviving ones are detailed in Tables 2.

7. RESULTS

7.1. Intrinsic Gravitational Wave Amplitude Upper Limits

No candidate survives the last stage hence there is no evidence for a continuous-wave signal from either targets.

We determine frequentist 90% confidence upper limits on the intrinsic GW amplitude in every half-Hz band, $h_0^{90\%}(f)$. $h_0^{90\%}(f)$ is the GW amplitude such that 90% of signals of our target population with that amplitude would have been detected by our search. To determine this value we measure the detection efficiency (or confidence) $C(h_0)$ on our target population at fixed values of h_0 and with a sigmoid fit we estimate the amplitude that yields 90% detection efficiency:

$$C(h_0) = \frac{1}{1 + \exp\left(\frac{a-h_0}{b}\right)}. \quad (12)$$

As for previous searches (J. Ming et al. 2019; M. A. Papa et al. 2020; J. Ming et al. 2022; J. Ming et al. 2024), MATLAB’s non-linear regression function, `nlpredi`, is used to determine the optimal values for coefficients a and b , along with the corresponding covariance matrix, based on which the 95% credible interval for the $h_0^{90\%}$ is derived. The fitting process introduces an uncertainty in $h_0^{90\%} \leq 5\%$ for most of the half-Hz bands. The total uncertainty in the upper limit is the sum of the fitting process uncertainty and LIGO’s calibration uncertainty, which we assume is 5 % (C. Cahillane et al. 2017).

The detection efficiency is the number of recovered signals relative to the total number of signals considered. Each test signal is added to the data and then the with the test signals is treated exactly like the data from original Einstein@Home search, including data preparation, cleaning and candidate-selection with pixeling. A signal is considered recovered if a result from the search with

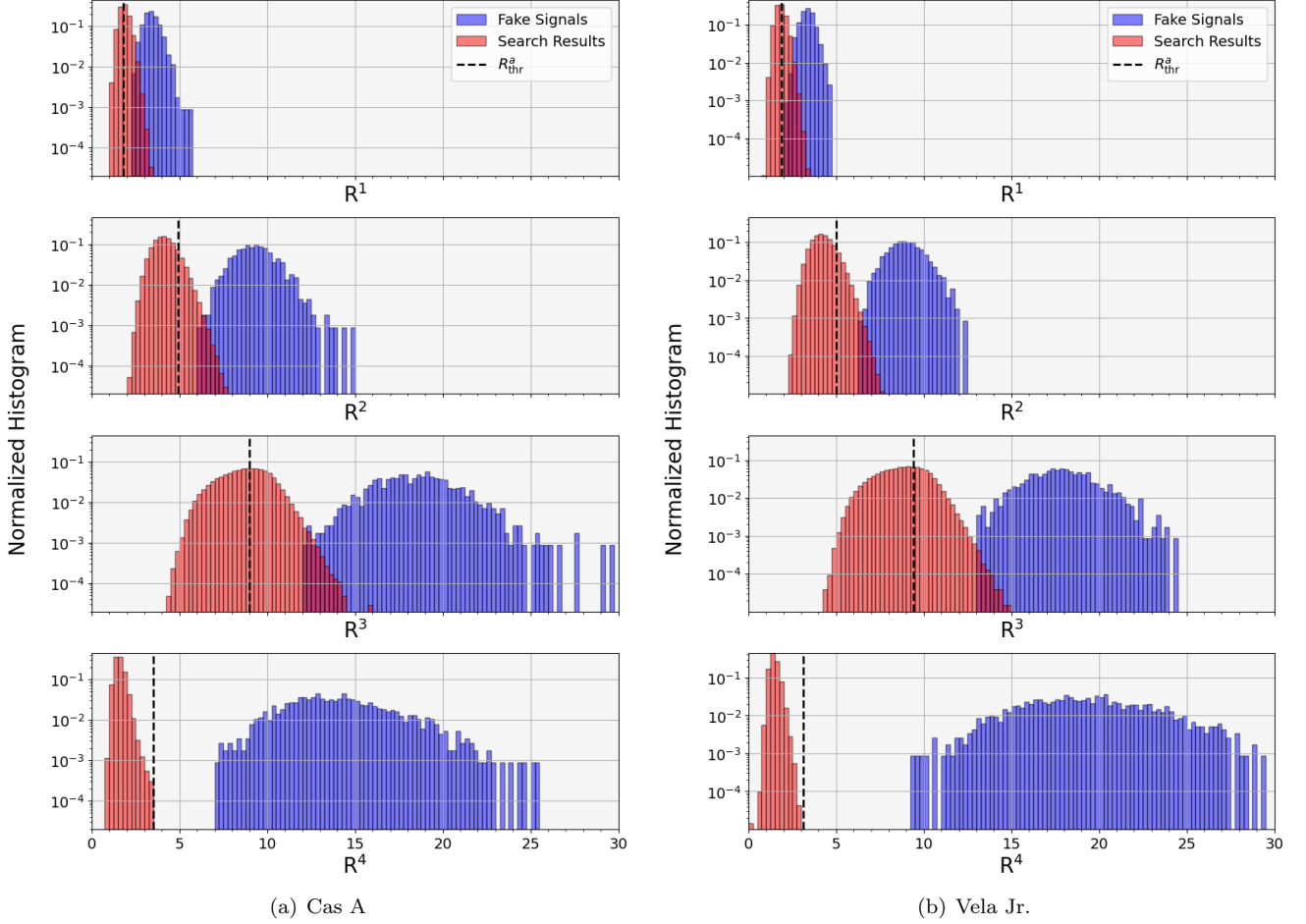


Figure 4. Distributions of R^a of the candidates from the searches (red, left) and from the target signal population (blue, right). The vertical dashed line shows the R^a_{thr} at each stage. One can see how the noise-dominated data and the test-signal population separate more and more clearly as the hierarchical follow-ups proceed, with the data containing signals moving to higher values of R .

the test signal, and ascribable to the signal, survives until the last stage. In practice, since the confidence in recovering signals at our upper limit amplitudes during the follow-up stages is much higher (99.96%) than the upper limit confidence level (90%) we neglect the false dismissal incurred by the follow-up and significantly simplify the upper limit pipeline by requiring that the test signal only survive Stage-0.

As described in Section 4, in frequency bands affected by large spectral-line disturbances, we substitute the real data with Gaussian noise. For consistency we also do this after the test signal has been added to noise, hence, depending on the data removed and on the frequency of the test signal, it might not be possible to reach the 90% confidence level for any value of h_0 . For frequency bands where this happens we do not provide upper limits. We add these bands to the list of excluded bands given in J. Ming et al. (2025). Such bands include 6 half-Hz bands between 20 Hz and 400 Hz and 109 half-

Hz bands between 400 Hz and 1700 Hz search, mostly due to the thermal excitation of vibration modes of the suspension silica fibers at 500 Hz and their harmonics around 1000 Hz and 1500 Hz (B. P. Abbott et al. 2016).

The $h_0^{90\%}$ upper limits for the Cas A and Vela Jr. searches lie in the upper 10^{-26} –low 10^{-25} range across the searched frequency bands, with the most stringent upper limit being 7.3×10^{-26} near 200 Hz for Cas A and near 400 Hz for Vela Jr. at 8.9×10^{-26} – see Figures 5. Both searches are by far the most sensitive on O2 data: our Cas A search is 4 times more sensitive than the previous O2 best sensitivity achieved by B. P. Abbott et al. (2019d), and our Vela Jr., search is 3 times more sensitive than B. P. Abbott et al. (2019d).

Searches carried out on the more sensitive O3 data provide more stringent constraints than ours: R. Abbott et al. (2022d) on Cas A and for Vela Jr. up to 976 Hz achieve an upper limit a factor $\lesssim 0.8$ smaller than ours, albeit with a factor of 1.6 more sensitive O3a. J. Wang &

K. Riles (2024) achieve the 1.6 sensitivity improvement using the larger full O3 data set, and searching a smaller 200 Hz band.

Above 976 Hz the Vela Jr. search presented here is the most sensitive search carried out to date.

7.2. Upper Limits Recast

We can re-cast the $h_0^{90\%}$ upper limits into equatorial ellipticity upper limits using (M. Zimmermann & E. Szedenis 1979)

$$\varepsilon = \frac{c^4}{4\pi^2} \frac{h_0 D}{I f^2}, \quad (13)$$

where c is the speed of light, G is the gravitational constant, and I is the moment of inertia of the neutron star with respect to its axis of rotation. We assume the conventional value of 10^{38} kg m² for I . We use the following distances for our targets: 200 pc and 900 pc for Vela Jr. and 3.4 kpc for Cas A. The results are shown in Figure 6 (a).

Additionally, we can re-cast the $h_0^{90\%}$ into upper limits for the r-mode amplitude (B. J. Owen 2010)

$$\alpha = 0.028 \left(\frac{h_0}{10^{-24}} \right) \left(\frac{D}{1 \text{ kpc}} \right) \left(\frac{100 \text{ Hz}}{f} \right)^3. \quad (14)$$

and show them in Figure 6 (b).

7.3. Sensitivity Depth

The sensitivity depth is a useful quantity first introduced by B. Behnke et al. (2015) to help compare different searches on data with the same noise level (C. Dreissigacker et al. 2018). The sensitivity depth is defined as

$$\mathcal{D}^{90\%}(f) \equiv \frac{\sqrt{S_n(f)}}{h_0^{90\%}(f)} [1/\sqrt{\text{Hz}}], \quad (15)$$

where $\sqrt{S_n(f)}$ is the noise level associated with the frequency of a putative signal. In essence, the sensitivity depth quantifies how deep the weakest detectable signal is buried into the noise floor. It depends on the search setup and on the post-processing of the results.

The average sensitivity depth across the frequency ranges is approximately $92[1/\sqrt{\text{Hz}}]$ for Cas A and $89[1/\sqrt{\text{Hz}}]$ for Vela Jr., respectively. Although the average mismatch of the original Einstein@Home search for the Vela Jr. is slightly smaller than for Cas A, the average sensitivity depth of search for Vela Jr. is slightly larger. The reason for this is that the follow-ups involve proportionally about 3.5 times more candidates for Cas A than for Vela Jr.

8. CONCLUSIONS

We present results for searches for continuous gravitational waves from the neutron star in the Cas A and Vela

Jr. supernova remnants. The considered waveforms cover frequencies in the range 20 - 400 Hz for Cas A and 400 - 1700Hz Vela Jr., and very broad frequency evolution scenarios including power-law frequency evolutions with braking indexes up to 7. In particular, the second-order spin-down range of our searches is $\ddot{f} \in [0, 7\dot{f}/\tau^2]$, which is broader than the range covered by R. Abbott et al. (2022d) and J. Wang & K. Riles (2024), who assume $[2|\dot{f}|^2/f, 7|\dot{f}|^2/f]$. Furthermore, our search range is independent of the template \dot{f} value, accommodating signals that deviate from a strict power law.

The large parameter space, comprising in all 1.3×10^{18} waveforms, could be investigated thanks to the computing power donated by the volunteers of the Einstein@Home project. Promising candidates across this space were identified using a new “pixeling” method and followed-up in a cascade of further searches. Fewer and fewer candidates survive each stage and at the end of the fourth stage no signal candidate is left, indicating no detectable signal.

We place upper limits on the intrinsic gravitational wave strain in half-Hz frequency bands. Comparing with the previous most sensitive search for Cas A in O2 data (B. P. Abbott et al. 2019d), our h_0 upper limit is significantly better by a factor of 4.

Due to the great sensitivity improvement of O3 data, on parts of the parameter space, our search is less sensitive than the two searches using O3a/O3 data (R. Abbott et al. 2022d; J. Wang & K. Riles 2024). However, when the difference in h_0 sensitivity between two searches for emission from young supernova remnants is quite small (tens of percent, not orders of magnitude, like in this case), carrying out a slightly less sensitive search on different data has value: Approximately 6% of pulsars are known to have experienced at least one glitch (S. Zhou et al. 2022), and glitches predominantly occur in young pulsars (M. Yu et al. 2013). Cas A is the youngest known supernova remnant in the Milky Way and its neutron star likely glitched since it was born roughly 330 years ago. If the Cas A neutron star glitched during the O3 run, the two O3 deep searches R. Abbott et al. (2022d) and J. Wang & K. Riles (2024) might well have missed the signal, which could have been instead picked up by this search because it did not employ a long coherence time on O3 data. The O3a Viterbi search for Cas A (R. Abbott et al. 2021a) is based on a hidden Markov model (L. Sun et al. 2018), which is more robust to glitches. Our search is complementary to that in that it is an order of magnitude more sensitive, as shown by the grey dots in Figure 5(a).

Below 976 Hz, the LVC O3a search for Vela Jr. (R. Abbott et al. 2022d) has a better sensitivity than ours

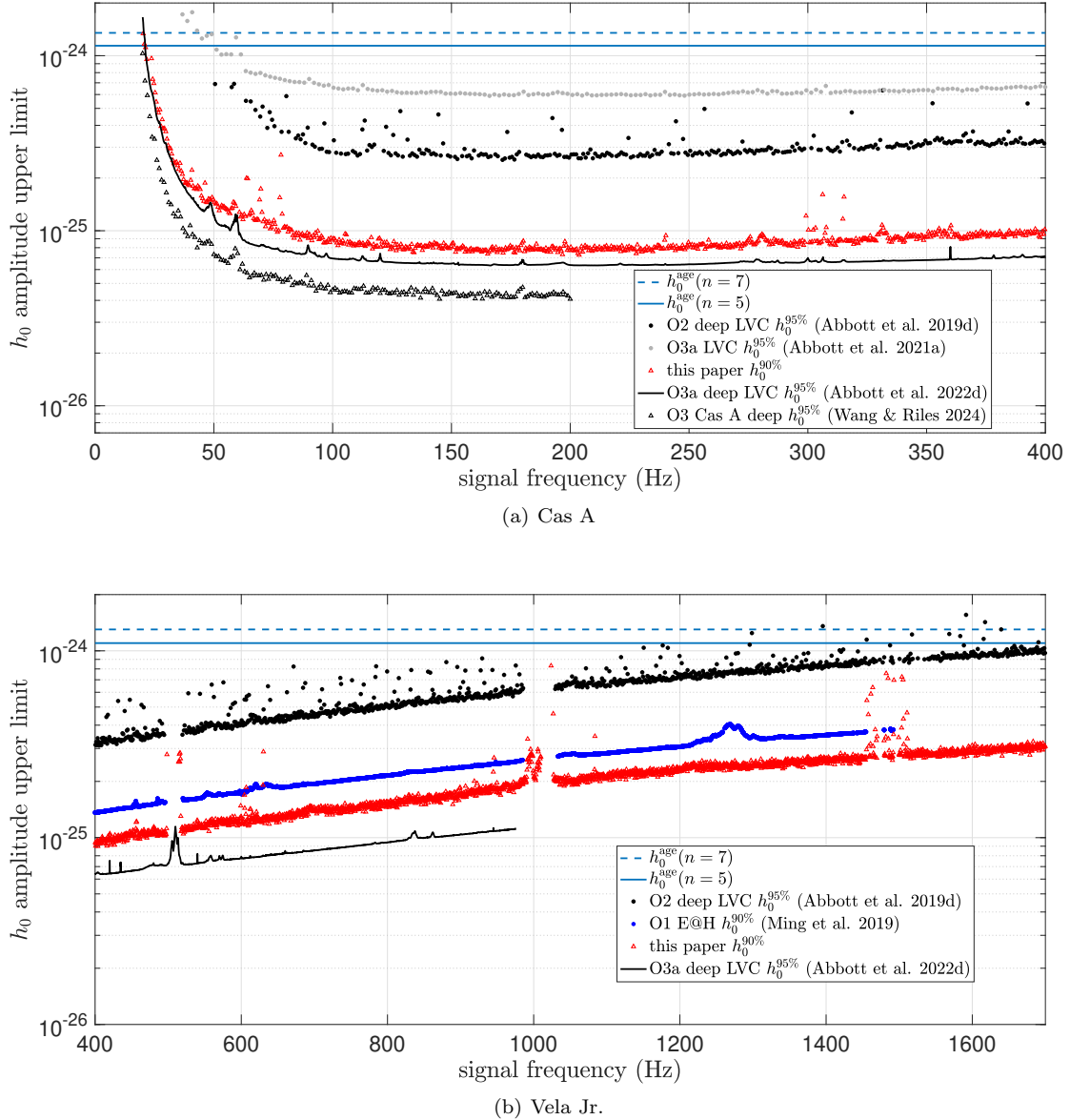


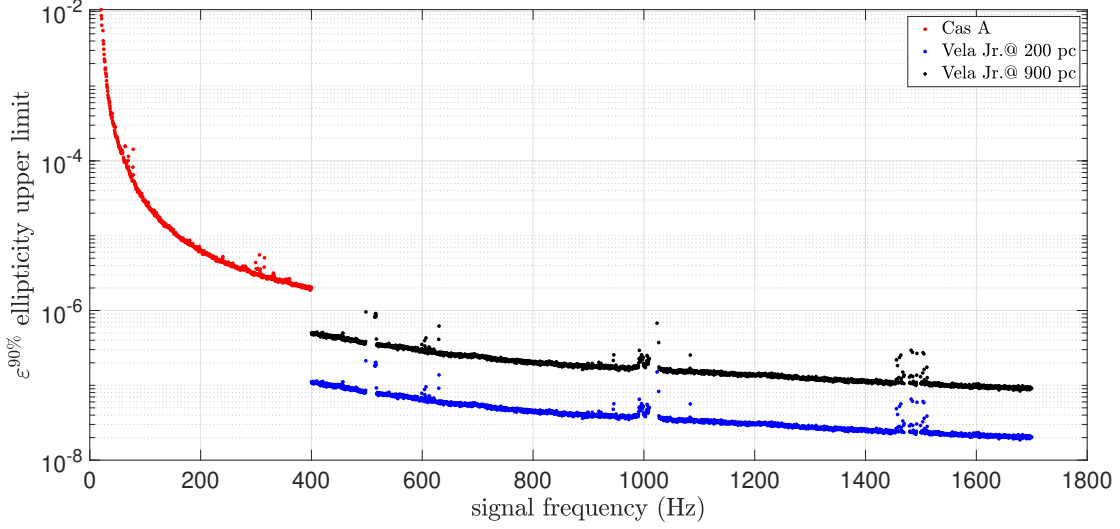
Figure 5. 90% confidence upper limits on the gravitational wave amplitude of continuous gravitational wave signals from our searches (red triangles) as a function of frequency, compared to other recent results. The horizontal lines show the indirect age-based upper limits corresponding to braking indexes of 5 and 7. Our searches could detect signals with n as high as 7.

by 30 %; Above 976 Hz the search presented here is the most sensitive search ever performed. It improves by 50% on our previous deep search (J. Ming et al. 2019) between 976 Hz and 1500 Hz, and above 1500 Hz it improves by 300% on the best previous result which was by B. P. Abbott et al. (2019d) also on O2 data.

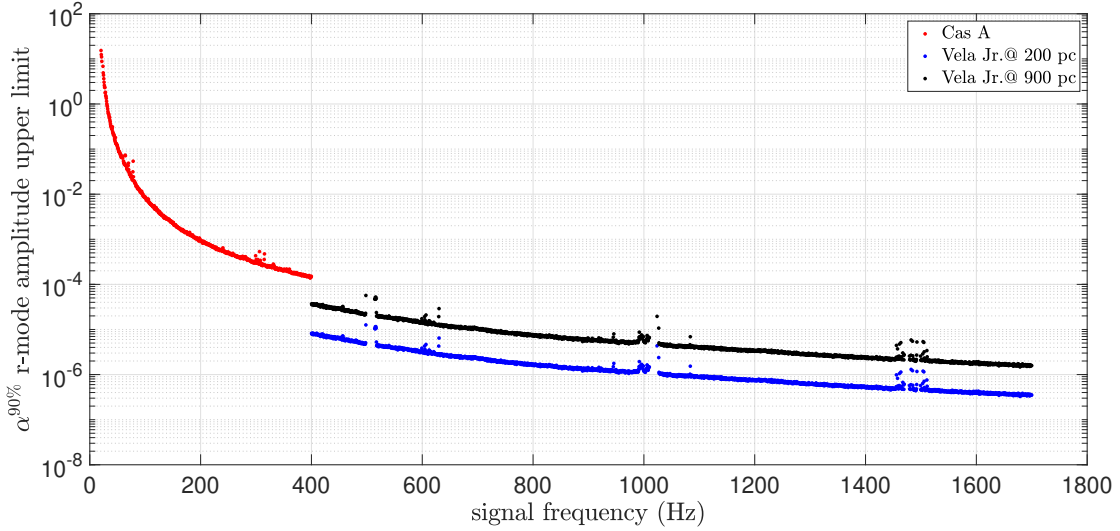
We recast the upper limits on the intrinsic strain into upper limits for both the equatorial ellipticity ε and the Newtonian r-mode amplitude (see Figures 6. For Cas A, $\varepsilon^{90\%}$ is constrained below 10^{-5} at the frequencies higher than ≈ 150 Hz, dropping to $< 2 \times 10^{-6}$ at 400 Hz. For Vela Jr., assuming a distance of 200 pc, our results

constrain $\varepsilon^{90\%}$ to be $< 10^{-7}$ for all investigated signal frequencies. At the highest frequency 1700 Hz, $\varepsilon^{90\%}$ is 2×10^{-8} . This is more than one order of magnitude lower than the physical plausible values predicted by N. Johnson-McDaniel & B. Owen (2013); F. Gittins et al. (2021); F. Gittins & N. Andersson (2021).

Newly-born neutron stars could present active r-modes oscillations, leading to continuous gravitational-wave emission and fast spin-down after collapse (P. Arzoumanian et al. 2003; B. J. Owen et al. 1998). Our search for Vela Jr. covers the r-mode emitting neutron star with a spin frequency up to ≈ 1275 Hz, and for Cas A up to a



(a) Upper limits on the ellipticity



(b) Upper limits on the r-mode amplitude

Figure 6. 90 % upper limits on the ellipticity (a) and r-mode amplitude (b) of the two targets. For Vela Jr. we show two curves, corresponding to two distance estimates: 200 pc and 900 pc. For Cas A, we assume 3400 pc.

spin frequency of ≈ 300 Hz. The expected r-mode amplitude α is quite small, with estimates ranging from 10^{-5} to 10^{-3} (R. Bondarescu et al. 2007; B. Haskell 2015). Our results for Cas A constrain $\alpha^{90\%}$ to be smaller than $\approx 10^{-3}$ above 200 Hz reaching $\approx 1 \times 10^{-4}$, at 400 Hz. For Vela Jr., assuming a distance of 200 pc, our results constrain $\alpha^{90\%}$ at 1700 Hz to be smaller than $\approx 3 \times 10^{-7}$, which well in the range of possible values.

9. ACKNOWLEDGMENTS

We gratefully acknowledge the support of the many thousands of Einstein@Home volunteers who made this search possible.

We acknowledge support from the Max Planck Society for Projects QPQ10003 and QPQ10004, and the NSF grant 1816904.

A lot of post-processing is run on the ATLAS cluster at AEI Hannover. We thank Carsten Aulbert and Henning Fehrmann for their support.

We would like to thank the instrument-scientist and engineers of LIGO whose amazing work has produced detectors capable of probing gravitational waves so incredibly small.

J.A.M. acknowledges the continuing support and guidance of Charles J. Horowitz, as well as partial support from the US Department of Energy grant

DE-FG02-87ER40365.

This research has made use of data, software and/or web tools obtained from the Gravitational Wave Open Science Center (<https://www.gw-openscience.org/>), a service of LIGO Laboratory, the LIGO Scientific Collaboration and the Virgo Collaboration. LIGO Laboratory and Advanced LIGO are funded by the United States National Science Foundation (NSF) as well as the Science and Technology Facilities Council (STFC) of the United Kingdom, the Max-Planck-Society (MPS), and the State of Niedersachsen/Germany for

support of the construction of Advanced LIGO and construction and operation of the GEO600 detector. Additional support for Advanced LIGO was provided by the Australian Research Council. Virgo is funded, through the European Gravitational Observatory (EGO), by the French Centre National de Recherche Scientifique (CNRS), the Italian Istituto Nazionale di Fisica Nucleare (INFN) and the Dutch Nikhef, with contributions by institutions from Belgium, Germany, Greece, Hungary, Ireland, Japan, Monaco, Poland, Portugal, Spain.

REFERENCES

- Abac, A. G., & other. 2025, <https://arxiv.org/abs/2501.01495>
- Abbott, B. P., et al. 2016, *Phys. Rev. D*, 94, 042002, doi: [10.1103/PhysRevD.94.042002](https://doi.org/10.1103/PhysRevD.94.042002)
- Abbott, B. P., et al. 2019a, *Phys. Rev. D*, 99, 122002, doi: [10.1103/PhysRevD.99.122002](https://doi.org/10.1103/PhysRevD.99.122002)
- Abbott, B. P., et al. 2019b, *ApJ*, 879, 10, doi: [10.3847/1538-4357/ab20cb](https://doi.org/10.3847/1538-4357/ab20cb)
- Abbott, B. P., et al. 2019c, *Phys. Rev. D*, 100, 122002, doi: [10.1103/PhysRevD.100.122002](https://doi.org/10.1103/PhysRevD.100.122002)
- Abbott, B. P., et al. 2019d, *The Astrophysical Journal*, 875, 122, doi: [10.3847/1538-4357/ab113b](https://doi.org/10.3847/1538-4357/ab113b)
- Abbott, R., et al. 2021a, *The Astrophysical Journal*, 921, 80, doi: [10.3847/1538-4357/ac17ea](https://doi.org/10.3847/1538-4357/ac17ea)
- Abbott, R., et al. 2021b, *SoftwareX*, 13, 012021, doi: <https://doi.org/10.1016/j.softx.2021.100658>
- Abbott, R., et al. 2022a, *The Astrophysical Journal*, 932, 133, doi: [10.3847/1538-4357/ac6ad0](https://doi.org/10.3847/1538-4357/ac6ad0)
- Abbott, R., et al. 2022b, *Phys. Rev. D*, 105, 022002, doi: [10.1103/PhysRevD.105.022002](https://doi.org/10.1103/PhysRevD.105.022002)
- Abbott, R., et al. 2022c, *Phys. Rev. D*, 106, 102008, doi: [10.1103/PhysRevD.106.102008](https://doi.org/10.1103/PhysRevD.106.102008)
- Abbott, R., et al. 2022d, *Phys. Rev. D*, 105, 082005, doi: [10.1103/PhysRevD.105.082005](https://doi.org/10.1103/PhysRevD.105.082005)
- Abbott, R., et al. 2022e, *Phys. Rev. D*, 106, 042003, doi: [10.1103/PhysRevD.106.042003](https://doi.org/10.1103/PhysRevD.106.042003)
- Abbott, R., et al. 2022f, *Astrophys. J. Lett.*, 941, L30, doi: [10.3847/2041-8213/aca1b0](https://doi.org/10.3847/2041-8213/aca1b0)
- Abbott, R., et al. 2022g, *Phys. Rev. D*, 105, 102001, doi: [10.1103/PhysRevD.105.102001](https://doi.org/10.1103/PhysRevD.105.102001)
- Abbott, R., et al. 2023, *The Astrophysical Journal Supplement Series*, 267, 29, doi: [10.3847/1538-4365/acdc9f](https://doi.org/10.3847/1538-4365/acdc9f)
- AEI. 2023,, <https://www.aei.mpg.de/25950/computer-clusters>
- Allen, G. E., Chow, K., DeLaney, T., et al. 2014, *The Astrophysical Journal*, 798, 82, doi: [10.1088/0004-637x/798/2/82](https://doi.org/10.1088/0004-637x/798/2/82)
- Anderson, D. 2004, in *Fifth IEEE/ACM International Workshop on Grid Computing*, 4–10, doi: [10.1109/GRID.2004.14](https://doi.org/10.1109/GRID.2004.14)
- Anderson, D. P., Christensen, C., & Allen, B. 2006, in *Proceedings of the 2006 ACM/IEEE Conference on Supercomputing, SC '06* (New York, NY, USA: Association for Computing Machinery), 126–es, doi: [10.1145/1188455.1188586](https://doi.org/10.1145/1188455.1188586)
- Andersson, N., Kokkotas, K. D., & Stergioulas, N. 1999, *The Astrophysical Journal*, 516, 307, doi: [10.1086/307082](https://doi.org/10.1086/307082)
- Arras, P., Flanagan, E. E., Morsink, S. M., et al. 2003, *The Astrophysical Journal*, 591, 1129, doi: [10.1086/374657](https://doi.org/10.1086/374657)
- Arvanitaki, A., Huang, J., & Van Tilburg, K. 2015, *Phys. Rev. D*, 91, 015015, doi: [10.1103/PhysRevD.91.015015](https://doi.org/10.1103/PhysRevD.91.015015)
- Ashok, A., Covas, P. B., Prix, R., & Papa, M. A. 2024, *Phys. Rev. D*, 109, 104002, doi: [10.1103/PhysRevD.109.104002](https://doi.org/10.1103/PhysRevD.109.104002)
- Ashok, A., Beheshtipour, B., Papa, M. A., et al. 2021, *The Astrophysical Journal*, 923, 85, doi: [10.3847/1538-4357/ac2582](https://doi.org/10.3847/1538-4357/ac2582)
- Behnke, B., Papa, M. A., & Prix, R. 2015, *Phys. Rev. D*, 91, 064007, doi: [10.1103/PhysRevD.91.064007](https://doi.org/10.1103/PhysRevD.91.064007)
- Bondarescu, R., Teukolsky, S. A., & Wasserman, I. 2007, *Phys. Rev. D*, 76, 064019, doi: [10.1103/PhysRevD.76.064019](https://doi.org/10.1103/PhysRevD.76.064019)
- Brady, P. R., & Creighton, T. 2000, *PhRvD*, 61, 082001, doi: [10.1103/PhysRevD.61.082001](https://doi.org/10.1103/PhysRevD.61.082001)
- Brady, P. R., Creighton, T., Cutler, C., & Schutz, B. F. 1998, *Phys. Rev. D*, 57, 2101, doi: [10.1103/PhysRevD.57.2101](https://doi.org/10.1103/PhysRevD.57.2101)
- Brown, E. F., & Ushomirsky, G. 2000, *The Astrophysical Journal*, 536, 915, doi: [10.1086/308969](https://doi.org/10.1086/308969)

- Cahillane, C., Betzwieser, J., Brown, D. A., et al. 2017, Phys. Rev. D, 96, 102001, doi: [10.1103/PhysRevD.96.102001](https://doi.org/10.1103/PhysRevD.96.102001)
- Clark, C. J., et al. 2023, Mon. Not. Roy. Astron. Soc., 519, 5590, doi: [10.1093/mnras/stac3742](https://doi.org/10.1093/mnras/stac3742)
- Covas, P. B., Papa, M. A., & Prix, R. 2024, <https://arxiv.org/abs/2409.16196>
- Covas, P. B., Papa, M. A., Prix, R., & Owen, B. J. 2022, The Astrophysical Journal Letters, 929, L19, doi: [10.3847/2041-8213/ac62d7](https://doi.org/10.3847/2041-8213/ac62d7)
- Dergachev, V., & Papa, M. 2020, Phys. Rev. Lett., 125, 171101, doi: [10.1103/PhysRevLett.125.171101](https://doi.org/10.1103/PhysRevLett.125.171101)
- Dergachev, V., & Papa, M. A. 2021, Phys. Rev. D, 104, 043003, doi: [10.1103/PhysRevD.104.043003](https://doi.org/10.1103/PhysRevD.104.043003)
- Dergachev, V., & Papa, M. A. 2023, Phys. Rev. X, 13, 021020, doi: [10.1103/PhysRevX.13.021020](https://doi.org/10.1103/PhysRevX.13.021020)
- Dergachev, V., Papa, M. A., Steltner, B., & Eggenstein, H.-B. 2019, Phys. Rev. D, 99, 084048, doi: [10.1103/PhysRevD.99.084048](https://doi.org/10.1103/PhysRevD.99.084048)
- Dreissigacker, C., Prix, R., & Wette, K. 2018, Phys. Rev. D, 98, 084058, doi: [10.1103/PhysRevD.98.084058](https://doi.org/10.1103/PhysRevD.98.084058)
- Einstein@Home. 2023,, <https://einsteinathome.org/>
- Fesen, R. A., Hammell, M. C., Morse, J., et al. 2006, The Astrophysical Journal, 645, 283, doi: [10.1086/504254](https://doi.org/10.1086/504254)
- Gittins, F., & Andersson, N. 2021, Monthly Notices of the Royal Astronomical Society, 507, 116, doi: [10.1093/mnras/stab2048](https://doi.org/10.1093/mnras/stab2048)
- Gittins, F., & Andersson, N. 2023, Monthly Notices of the Royal Astronomical Society, 521, 3043, doi: [10.1093/mnras/stad672](https://doi.org/10.1093/mnras/stad672)
- Gittins, F., Andersson, N., & Jones, D. 2021, Mon. Notices Royal Astron. Soc., 500, 5570, doi: [10.1093/mnras/staa3635](https://doi.org/10.1093/mnras/staa3635)
- Haskell, B. 2015, Int. J. Mod. Phys. E, 24, 1541007, doi: [10.1142/S0218301315410074](https://doi.org/10.1142/S0218301315410074)
- Haskell, B., Glampedakis, K., & Andersson, N. 2014, Monthly Notices of the Royal Astronomical Society, 441, 1662, doi: [10.1093/mnras/stu535](https://doi.org/10.1093/mnras/stu535)
- Haskell, B., Jones, D. I., & Andersson, N. 2006, Monthly Notices of the Royal Astronomical Society, 373, 1423, doi: [10.1111/j.1365-2966.2006.10998.x](https://doi.org/10.1111/j.1365-2966.2006.10998.x)
- Ho, W., & Heinke, C. 2009, Nature, 462, 71, doi: [10.1038/nature08525](https://doi.org/10.1038/nature08525)
- Horowitz, C., Papa, M., & Reddy, S. 2020, Physics Letters B, 800, 135072, doi: <https://doi.org/10.1016/j.physletb.2019.135072>
- Horowitz, C. J., & Reddy, S. 2019, Phys. Rev. Lett., 122, 071102, doi: [10.1103/PhysRevLett.122.071102](https://doi.org/10.1103/PhysRevLett.122.071102)
- Hutchins, T. J., & Jones, D. I. 2023, Monthly Notices of the Royal Astronomical Society, 522, 226, doi: [10.1093/mnras/stad967](https://doi.org/10.1093/mnras/stad967)
- Iyudin, A. F., Schoenfelder, V., Bennett, K., et al. 1998, Nature, 396, 142, doi: [10.1038/24106](https://doi.org/10.1038/24106)
- Jaranowski, P., Królak, A., & Schutz, B. F. 1998, Phys. Rev. D, 58, 063001, doi: [10.1103/PhysRevD.58.063001](https://doi.org/10.1103/PhysRevD.58.063001)
- Johnson-McDaniel, N., & Owen, B. 2013, Phys. Rev. D, 88, 044004
- Keitel, D. 2016, Phys. Rev., D93, 084024, doi: [10.1103/PhysRevD.93.084024](https://doi.org/10.1103/PhysRevD.93.084024)
- Keitel, D., Prix, R., Papa, M. A., Leaci, P., & Siddiqi, M. 2014, doi: [10.1103/PhysRevD.89.064023](https://doi.org/10.1103/PhysRevD.89.064023)
- Lindblom, L., & Owen, B. J. 2020, Phys. Rev. D, 101, 083023, doi: [10.1103/PhysRevD.101.083023](https://doi.org/10.1103/PhysRevD.101.083023)
- Mignani, R. P., De Luca, A., Zaggia, S., et al. 2007, Astronomy and Astrophysics, 473, 883, doi: [10.1051/0004-6361:20077768](https://doi.org/10.1051/0004-6361:20077768)
- Miller, A. L., Aggarwal, N., Clesse, S., et al. 2024, Phys. Rev. Lett., 133, 111401, doi: [10.1103/PhysRevLett.133.111401](https://doi.org/10.1103/PhysRevLett.133.111401)
- Millhouse, M., Strang, L., & Melatos, A. 2020, Phys. Rev. D, 102, 083025, doi: [10.1103/PhysRevD.102.083025](https://doi.org/10.1103/PhysRevD.102.083025)
- Ming, J., Krishnan, B., Papa, M. A., Aulbert, C., & Fehrmann, H. 2016, Phys. Rev. D, 93, 064011, doi: [10.1103/PhysRevD.93.064011](https://doi.org/10.1103/PhysRevD.93.064011)
- Ming, J., Papa, M. A., Eggenstein, H. B., et al. 2024, ApJ, 977, 154, doi: [10.3847/1538-4357/ad8b9e](https://doi.org/10.3847/1538-4357/ad8b9e)
- Ming, J., Papa, M. A., Eggenstein, H.-B., et al. 2022, The Astrophysical Journal, 925, 8, doi: [10.3847/1538-4357/ac35cb](https://doi.org/10.3847/1538-4357/ac35cb)
- Ming, J., Papa, M. A., Krishnan, B., et al. 2018, Phys. Rev. D, 97, 024051, doi: [10.1103/PhysRevD.97.024051](https://doi.org/10.1103/PhysRevD.97.024051)
- Ming, J., Papa, M. A., Singh, A., et al. 2019, Phys. Rev. D, 100, 024063, doi: [10.1103/PhysRevD.100.024063](https://doi.org/10.1103/PhysRevD.100.024063)
- Ming, J., et al. 2025, www.aei.mpg.de/continuouswaves/o2_casa_velajr_deep-directedsearches
- Mirasola, L., et al. 2024, Phys. Rev. D, 110, 123043, doi: [10.1103/PhysRevD.110.123043](https://doi.org/10.1103/PhysRevD.110.123043)
- Mirasola, L., et al. 2025, <https://arxiv.org/abs/2501.02052>
- Morales, J. A., & Horowitz, C. J. 2022, Monthly Notices of the Royal Astronomical Society, 517, 5610, doi: [10.1093/mnras/stac3058](https://doi.org/10.1093/mnras/stac3058)
- Morales, J. A., & Horowitz, C. J. 2024, Phys. Rev. D, 110, 044016, doi: [10.1103/PhysRevD.110.044016](https://doi.org/10.1103/PhysRevD.110.044016)
- Nieder, L., et al. 2020, Astrophys. J. Lett., 902, L46, doi: [10.3847/2041-8213/abbc02](https://doi.org/10.3847/2041-8213/abbc02)
- Owen, B. J. 2010, Phys. Rev. D, 82, 104002, doi: [10.1103/PhysRevD.82.104002](https://doi.org/10.1103/PhysRevD.82.104002)

- Owen, B. J., Lindblom, L., Cutler, C., et al. 1998, doi: [10.1103/PhysRevD.58.084020](https://doi.org/10.1103/PhysRevD.58.084020)
- Owen, B. J., Lindblom, L., & Pinheiro, L. S. 2022, *The Astrophysical Journal Letters*, 935, L7, doi: [10.3847/2041-8213/ac84dc](https://doi.org/10.3847/2041-8213/ac84dc)
- Owen, B. J., Lindblom, L., Pinheiro, L. S., & Rajbhandari, B. 2024, *Astrophys. J. Lett.*, 962, L23, doi: [10.3847/2041-8213/ad2263](https://doi.org/10.3847/2041-8213/ad2263)
- Papa, M. A., Ming, J., Gotthelf, E. V., et al. 2020, *The Astrophysical Journal*, 897, 22, doi: [10.3847/1538-4357/ab92a6](https://doi.org/10.3847/1538-4357/ab92a6)
- Pavlov, G. G., Sanwal, D., Kiziltan, B., & Garmire, G. P. 2001, *The Astrophysical Journal*, 559, L131, doi: [10.1086/323975](https://doi.org/10.1086/323975)
- Piccinni, O. J., Astone, P., D’Antonio, S., et al. 2020, *Phys. Rev. D*, 101, 082004, doi: [10.1103/PhysRevD.101.082004](https://doi.org/10.1103/PhysRevD.101.082004)
- Pletsch, H. J. 2008, *Phys. Rev. D*, 78, 102005, doi: [10.1103/PhysRevD.78.102005](https://doi.org/10.1103/PhysRevD.78.102005)
- Pletsch, H. J. 2010, *Phys. Rev. D*, 82, 042002, doi: [10.1103/PhysRevD.82.042002](https://doi.org/10.1103/PhysRevD.82.042002)
- Pletsch, H. J., & Allen, B. 2009, *Phys. Rev. Lett.*, 103, 181102, doi: [10.1103/PhysRevLett.103.181102](https://doi.org/10.1103/PhysRevLett.103.181102)
- Rajbhandari, B., Owen, B. J., Caride, S., & Inta, R. 2021, *Phys. Rev. D*, 104, 122008, doi: [10.1103/PhysRevD.104.122008](https://doi.org/10.1103/PhysRevD.104.122008)
- Reed, J. E., Hester, J. J., Fabian, A. C., & Winkler, P. F. 1995, *ApJ*, 440, 706, doi: [10.1086/175308](https://doi.org/10.1086/175308)
- Singh, A., & Papa, M. A. 2023, *Astrophys. J.*, 943, 99, doi: [10.3847/1538-4357/acaf80](https://doi.org/10.3847/1538-4357/acaf80)
- Singh, A., Papa, M. A., Eggenstein, H.-B., & Walsh, S. 2017, *Phys. Rev. D*, 96, 082003, doi: [10.1103/PhysRevD.96.082003](https://doi.org/10.1103/PhysRevD.96.082003)
- Steltner, B., Menne, T., Papa, M. A., & Eggenstein, H.-B. 2022a, *Phys. Rev. D*, 106, 104063, doi: [10.1103/PhysRevD.106.104063](https://doi.org/10.1103/PhysRevD.106.104063)
- Steltner, B., Papa, M. A., & Eggenstein, H.-B. 2022b, *Phys. Rev. D*, 105, 022005, doi: [10.1103/PhysRevD.105.022005](https://doi.org/10.1103/PhysRevD.105.022005)
- Steltner, B., Papa, M. A., Eggenstein, H.-B., et al. 2023, *The Astrophysical Journal*, 952, 55, doi: [10.3847/1538-4357/acdad4](https://doi.org/10.3847/1538-4357/acdad4)
- Sun, L., Melatos, A., Suvorova, S., Moran, W., & Evans, R. J. 2018, *Phys. Rev. D*, 97, 043013, doi: [10.1103/PhysRevD.97.043013](https://doi.org/10.1103/PhysRevD.97.043013)
- Tananbaum, H. 1999, *IAU Circulars*, 7246, 1
- Ushomirsky, G., Cutler, C., & Bildsten, L. 2000, *Mon. Notices Royal Astron. Soc.*, 319, 902, doi: [10.1046/j.1365-8711.2000.03938.x](https://doi.org/10.1046/j.1365-8711.2000.03938.x)
- Vargas, A. F., & Melatos, A. 2024, *Mon. Not. Roy. Astron. Soc.*, 534, 3410, doi: [10.1093/mnras/stae2326](https://doi.org/10.1093/mnras/stae2326)
- Wang, J., & Riles, K. 2024, *Phys. Rev. D*, 110, 042006, doi: [10.1103/PhysRevD.110.042006](https://doi.org/10.1103/PhysRevD.110.042006)
- Wette, K., Owen, B. J., Allen, B., et al. 2008, *Classical and Quantum Gravity*, 25, 235011, doi: [10.1088/0264-9381/25/23/235011](https://doi.org/10.1088/0264-9381/25/23/235011)
- Yu, M., Manchester, R. N., Hobbs, G., et al. 2013, *MNRAS*, 429, 688, doi: [10.1093/mnras/sts366](https://doi.org/10.1093/mnras/sts366)
- Zhang, Y., Papa, M. A., Krishnan, B., & Watts, A. L. 2021, *The Astrophysical Journal Letters*, 906, L14, doi: [10.3847/2041-8213/abd256](https://doi.org/10.3847/2041-8213/abd256)
- Zhou, S., Gügercinoğlu, E., Yuan, J., Ge, M., & Yu, C. 2022, *Universe*, 8, 641, doi: [10.3390/universe8120641](https://doi.org/10.3390/universe8120641)
- Zhu, S. J., Baryakhtar, M., Papa, M. A., et al. 2020, *Phys. Rev. D*, 102, 063020, doi: [10.1103/PhysRevD.102.063020](https://doi.org/10.1103/PhysRevD.102.063020)
- Zimmermann, M., & Szedenits, E. 1979, *Phys. Rev. D*, 20, 351, doi: [10.1103/PhysRevD.20.351](https://doi.org/10.1103/PhysRevD.20.351)